Zitierweise: *Angew. Chem. Int. Ed.* **2025**, *64*, e202516059
doi.org/10.1002/anie.202516059

Aluminum Batteries | Very Important Paper

$AlCl_4^-$-Deficient Eutectic Electrolytes Enable Reversible Iodine Redox-Amphoteric Conversion for Aluminum Battery Cathodes

*Xingyuan Chu[+], Shengyue Lu[+], Shaik Ghouse[+], Jiaxu Zhang, Arafat Hossain Khan, Jingwei Du, Xiaodong Li, Buyun Gao, Xiaohui Liu, Ahiud Morag, Xinmei Song, Dongqi Li, Leilei Zheng, Quanquan Guo, Mingchao Wang, Eike Brunner, Xinliang Feng, and Minghao Yu**

Abstract: Aluminum (Al) batteries are promising for sustainable and large-scale energy storage due to the inherent safety, low cost, and attractive metrics of the Al anode. However, the development of high-voltage and high-capacity cathodes remains a key challenge. Herein, we achieve the reversible iodine redox-amphoteric conversion (i.e., $I^-/I^0/I^+$) in Al batteries, wherein $AlCl_4^-$-deficient eutectic electrolytes are identified critical for stabilizing the conversion process. In contrast to ionic liquid electrolytes prone to parasitic Cl_2 evolution, eutectic systems facilitate the $I^-/I^0/I^+$ conversion process with high reversibility and significantly suppressed Cl_2 generation. Spectroscopic and theoretical investigations reveal $AlCl_4^-$ as the dominant species limiting anodic stability of the electrolyte, and its reduced presence in eutectic electrolytes directly enhances iodine conversion reversibility. The optimized electrolyte allows the I_2 electrode to deliver a specific capacity of 358 mAh g^{-1} and an energy density of 490 Wh kg^{-1} (based on I_2 mass), along with excellent cycling stability (83.8% retention over 1000 cycles). High-loading I_2 electrodes (8.52 mg cm^{-2}) achieve a high areal capacity of 2.25 mAh cm^{-2} and demonstrate practical feasibility in a single-layer pouch cell. This work establishes a new design framework for high-energy-density Al batteries and opens avenues for advancing conversion chemistries in multivalent systems.

Introduction

Aluminum (Al) batteries have gained intensive attention as a promising next-generation energy storage solution, benefiting from the direct utilization of Al metal as the anode.[1–5] Al is the most abundant metal element in the Earth's crust (8.23%) and is thus economically attractive (1.9 USD kg^{-1}).[6] Reversible Al stripping/plating is typically achieved in ionic liquid or eutectic electrolytes, where $Al_2Cl_7^-$ and/or $AlCl_2^+$ serve as the active species for Al metal deposition.[7–10] Due to its trivalent charge and high mass density (2.7 g cm^{-3}), the Al anode delivers an exceptional theoretical gravimetric capacity of 2980 mAh g^{-1} and a volumetric capacity of 8046 mAh cm^{-3}.[11–13] Moreover, Al metal deposition is inherently dendrite-free, significantly mitigating short-circuit risks and enhancing the overall safety of Al batteries.[14–16]

Nevertheless, the full potential of Al batteries is hindered by the lack of suitable cathode materials that ideally combine high specific capacity and elevated discharge voltage.[17] A variety of materials have been explored as potential cathodes for Al batteries. Among them, carbonous materials like graphite and graphene currently stand for the state-of-the-art, relying on reversible intercalation or adsorption of anionic species, typically $AlCl_4^-$.[8,11] Despite their excellent rate capability and decent discharge voltage, the practical application of carbonaceous materials is constrained by intrinsically low specific capacities (< 130 mAh g^{-1}). In addition, efforts have been made to develop cathodes that store cationic species (e.g., Al^{3+}, $AlCl_2^+$), including intercalation-type transition metal

[*] X. Chu[+], S. Lu[+], S. Ghouse[+], J. Zhang, J. Du, Dr. X. Li, X. Liu, Dr. A. Morag, Dr. X. Song, Dr. D. Li, L. Zheng, Dr. Q. Guo, Prof. X. Feng, Dr. M. Yu
Center for Advancing Electronics Dresden (cfaed) & Faculty of Chemistry and Food Chemistry, Technische Universität Dresden 01069, Dresden, Germany
E-mail: minghao.yu@tu-dresden.de

Dr. A. H. Khan, B. Gao, Prof. E. Brunner
Chair of Bioanalytical Chemistry, Technische Universität Dresden 01062, Dresden, Germany

Dr. X. Li, Prof. X. Feng, Dr. M. Yu
Department of Synthetic Materials and Functional Devices, Max Planck Institute of Microstructure Physics 06120, Halle, Germany

Dr. A. Morag
Department of Chemical Engineering, Ben-Gurion University of the Negev, Beer-Sheva 8410501, Israel

Dr. M. Wang
Guangdong Provincial Key Laboratory of Nano-Micro Materials Research & State Key Laboratory of Advanced Waterproof Materials, School of Advanced Materials, Peking University Shenzhen Graduate School, Shenzhen 518055, China

[+] These authors contributed equally to this work.

Additional supporting information can be found online in the Supporting Information section

compounds,[18] conversion-type chalcogens/chalcogenides,[19] and coordination-type organic materials.[20] However, these materials often suffer from sluggish reaction kinetics and rapid structural degradation, primarily due to the complex, charge-dense nature of the cationic charge carriers.[21,22] As a result, such electrodes typically experience pronounced charge/discharge polarization and poor cycling stability, restricting their practical viability in Al batteries.

Owing to the reversible conversion chemistry and natural abundance, iodine (I_2) has emerged as a promising cathode material option for a wide range of battery systems. In particular, the typical I^-/I° conversion endows I_2 with a theoretical specific capacity of 211 mAh g−1 and a conversion potential of 0.53 V versus standard hydrogen electrode (SHE).[23] This conversion reaction has been extensively explored in non-aqueous Li-ion batteries,[24] Na-ion batteries,[25] K-ion batteries,[26] and aqueous Zn batteries,[27] with significant efforts devoted to electrolyte optimization and the development of stable I_2 host materials. Recently, Han et al. extended the I^-/I° conversion to non-aqueous Al batteries, achieving a capacity exceeding 200 mAh g^{-1} and stable cycling performance over 150 cycles by employing a polyvinylpyrrolidone host to effectively suppress the shuttle effect of dissolved polyiodides.[28] A promising approach to further enhance the performance of I_2 cathodes is to activate an additional I^0/I^+ conversion step, typically triggered by the participation of guest anions (e.g., Cl^-). This I^0/I^+ conversion can not only double the theoretical specific capacity of I_2 to 422 mAh g−1 but also significantly elevate the average discharge voltage by introducing an additional conversion potential at 1.07 V versus SHE. For instance, the energy density of a Zn//I_2 battery increased from 314 Wh kg^{-1} (based on the mass of I_2) via the I^-/I° conversion to 700 Wh kg^{-1} via the full $I^-/I^0/I^+$ conversion.[29] In this context, extending the $I^-/I^0/I^+$ conversion chemistry to the emerging Al battery system presents a highly compelling yet unexplored opportunity.

In this work, we successfully activate the iodine redox-amphoteric conversion ($I^-/I^0/I^+$) in Al batteries, with $AlCl_4^-$-deficient eutectic electrolytes identified as essential for ensuring electrochemical reversibility. Specifically, we investigate the iodine conversion behavior in two typical classes of Al battery electrolytes: ionic liquid electrolytes (Figure 1a, $AlCl_3$/EMIMCl (1-ethyl-3-methylimidazolium chloride) as the representative) and eutectic electrolytes (Figure 1b, $AlCl_3$/acetamide as the representative). While partial $I^-/I^0/I^+$ conversion is observed in ionic liquid electrolytes, it is accompanied by severe parasitic reactions with Cl_2 gas formation, which result in low Coulombic efficiencies (e.g., 57.9% for $AlCl_3$/EMIMCl). By contrast, eutectic electrolytes enable complete and reversible $I^-/I^0/I^+$ conversion, with $AlCl_3$/acetamide reaching a high Coulombic efficiency of 92.4%. Using the $AlCl_3$/acetamide electrolyte, the I_2 cathode delivers a large specific capacity of 358 mAh g^{-1} and an energy density of 490 Wh kg^{-1} (based on I_2 mass), outperforming most reported cathode materials for Al batteries. It also exhibits good cycling stability, retaining 83.8% of the initial capacity after 1000 cycles at 1 A g^{-1}. This excellent reversibility is attributed to the wide anodic stability window in eutectic electrolytes (e.g., 2.43 V versus Al for $AlCl_3$/acetamide, 2.30 V versus Al for $AlCl_3$/EMIMCl). Computational simulations and spectroscopy investigation identify $AlCl_4^-$ as the decisive species governing electrolyte anodic stability, as indicated by its highest occupied molecular orbital (HOMO) energy level among all identified electrolyte species. Compared with ionic liquid electrolytes (0.29 mol L^{-1} for $AlCl_3$/EMIMCl), eutectic electrolytes (0.09 mol L^{-1} for $AlCl_3$/acetamide) contain significantly less anodic species, especially $AlCl_4^-$, thus offering higher anodic tolerance compatible with the full $I^-/I^0/I^+$ conversion. In addition, the high conversion kinetics allows for constructing high-loading I_2 cathodes (up to 8.52 mg cm^{-2}), which achieve a state-of-the art areal capacity of 2.25 mAh cm^{-2}. A single-layer pouch cell built with this electrode demonstrates stable performance over 100 cycles, highlighting its practicability for future energy storage applications.

Results and Discussion

Initiation of Iodine Redox-Amphoteric Conversion

We fabricated the I_2 electrode by using Ketjenblack carbon, a conductive carbon material with a high specific surface area, as the matrix to host active I_2. The prepared I_2 electrode exhibited stable iodine loading without noticeable sublimation (Figure S1), ensuring reliable mass utilization during electrochemical testing. A standard electrode with an iodine mass loading of ∼2 mg cm^{-2} was initially investigated in four electrolytes, including ionic-liquid ($AlCl_3$/EMIMCl and $AlCl_3$/BMIMCl (1-butyl-3-methylimidazolium chloride) with a molar ratio of 1.3) and eutectic systems ($AlCl_3$/acetamide and $AlCl_3$/urea with a molar ratio of 1.3). All four electrolytes exhibited high Al stripping/plating kinetics and reversibility (Figures S2–3). Electrochemical performance of the I_2 electrodes was assessed in two-electrode Swagelok cells with Al foil as the counter electrodes.

Galvanostatic charge–discharge (GCD) measurements were performed at 1 A g^{-1} with varying cutoff voltages in $AlCl_3$/EMIMCl (Figure 2a), $AlCl_3$/BMIMCl (Figure S4), $AlCl_3$/acetamide (Figure 2b), and $AlCl_3$/urea (Figure S5). With a cutoff voltage of 1.6 V, all systems exhibited a single pair of charge–discharge plateaus around 0.9 ∼ 1.4 V versus Al, corresponding to the I^-/I° conversion.[28] Increasing the cutoff voltage to 2.25 V revealed a second pair of charge–discharge plateaus, indicative of I^0/I^+ conversion. However, this process showed poor reversibility in ionic liquid electrolytes, with Coulombic efficiencies of only 57.9% in $AlCl_3$/EMIMCl and 56.3% in $AlCl_3$/BMIMCl. In situ Raman spectroscopy was performed to understand the low Coulombic efficiency in $AlCl_3$/EMIMCl. In comparison with the pristine state, the electrolyte after 10 charge–discharge cycles exhibits a pronounced Raman peak at 558 cm^{-1} (Figure 2c), corresponding to the symmetric stretching vibration of Cl_2.[30,31] This observation indicates that side reaction in $AlCl_3$/EMIMCl leads to Cl_2 generation, likely originating from uncontrolled oxidative decomposition of the electrolyte. Moreover, the cyclic voltammetry (CV) result of the I_2 electrodes in these four electrolytes further verified these findings (Figure S6).

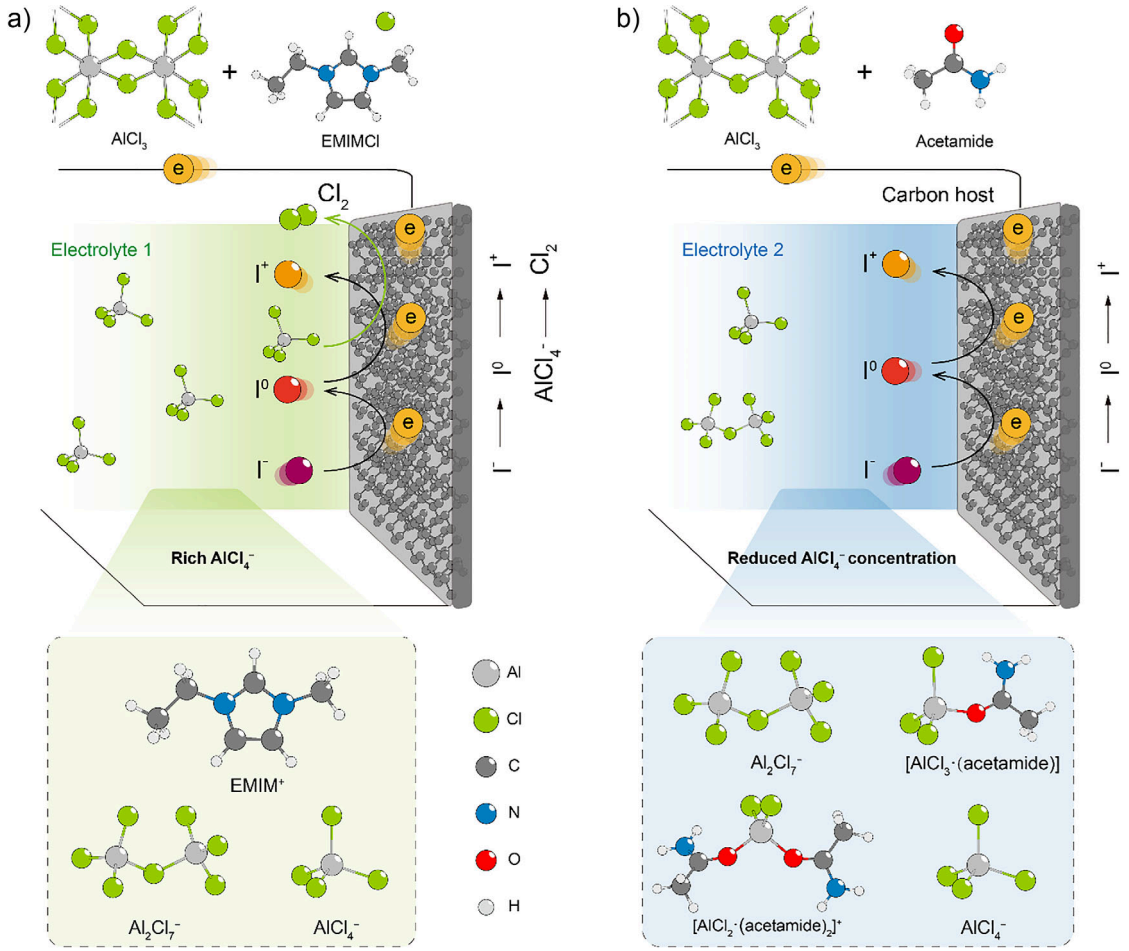

Figure 1. Schematic of the I_2 electrode with iodine redox- amphiprotic conversion. a) Iodine conversion and severe Cl_2 generation in an ionic liquid electrolyte ($AlCl_3$/EMIMCl) with rich $AlCl_4^-$. b) Iodine conversion in a eutectic electrolyte ($AlCl_3$/acetamide) with reduced $AlCl_4^-$ concentration.

By contrast, eutectic electrolytes enabled high reversibility of the iodine conversion reaction, achieving Coulombic efficiencies of 92.4% in $AlCl_3$/acetamide and 92.2% in $AlCl_3$/urea. Using the optimal $AlCl_3$/acetamide electrolyte, the I_2 electrode reached an overall specific capacity of 358 mAh g^{-1}. Control experiments confirmed that the capacity contribution from the Ketjenblack carbon host was negligible (Figure S7). In situ Raman spectra further verified the successful activation of the reversible $I^-/I^0/I^+$ conversion in $AlCl_3$/acetamide (Figure 2d). Specifically, at the fully discharged state (0.3 V), no Raman peaks were detected within the range of 60 ~ 270 cm^{-1}, consistent with complete reduction of I_2 to I^-.[28,32] Upon charging, two characteristic peaks emerged: one at 108 cm^{-1} corresponding to I_3^- and the other at 168 cm^{-1} attributed to the symmetric stretching vibration of molecular I_2.[33] As the voltage increased to 2.25 V, the I_3^- and I_2 peaks disappeared, and a new peak at 195 cm^{-1} appeared, matching the Raman signature of ICl (Figure S8)[29,34] and confirming ICl as the final charged product. During discharge, the ICl signal gradually diminished, while the I_2 and I_3^- peaks appeared. Eventually, all Raman signals vanished at the end of discharge, indicating full conversion back to I^- and excellent reversibility of the iodine redox-amphoteric conversion. Likely, I K-edge X-ray absorption near-edge structure (XANES) spectra identified the presence of I^+ in the fully charged I_2 electrode (Figure 2e). Compared with the original I_2 electrode, the fully charged I_2 electrode exhibits a negatively shifted edge energy, which aligns with the lower edge energy of the ICl reference than that of the I_2 reference (Figure S9). This shift can be attributed to the nature of the final electronic states involved in XANES transitions.[35] Specifically, I K-edge corresponds to the electronic excitation from the 1s orbital to the 5p orbital.[36] Upon oxidation, both the 1s level and the final-state energy of I are lowered, with a more pronounced decrease in the latter. Consequently, the energy gap between the initial and final states is reduced, resulting in a negative shift of the absorption edge.

We further conducted ab initio molecular dynamics (AIMD) simulations to shed light on the potential charge-compensating cations for I^- in the fully discharged I_2 electrode. Specifically, an I^- anion was introduced into the $AlCl_3$/acetamide electrolyte with a simulation box of 2 nm × 2 nm × 2 nm (Figure 2f). Analysis of the simulation trajectory revealed that two $[AlCl_2{\cdot}(acetamide)_2]^+$ species are closely associated with the I^- anion (Figure 2g). Radial distribution function (RDF) analysis indicates the coordination between I^- and Al atoms from the $[AlCl_2{\cdot}(acetamide)_2]^+$

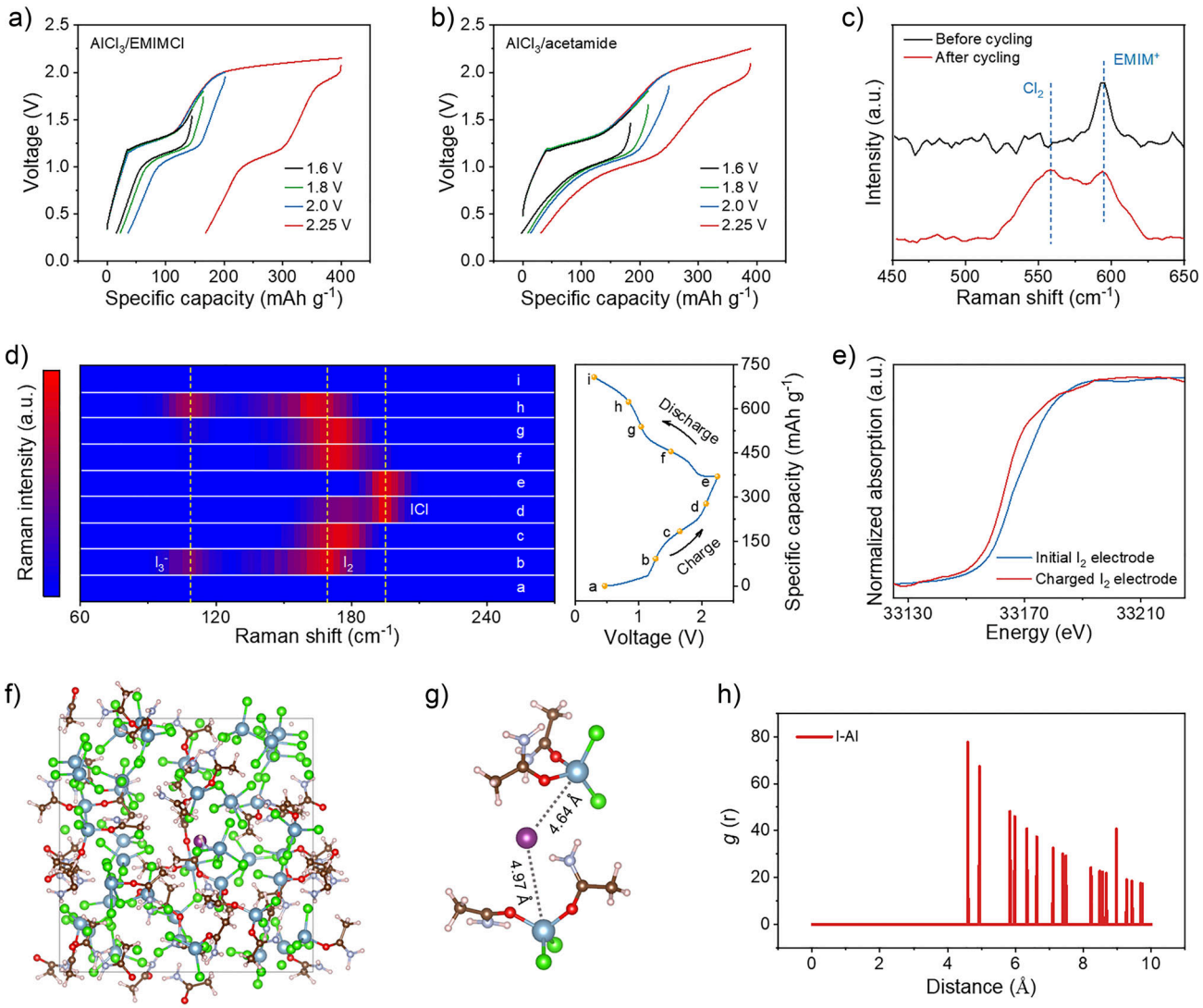

Figure 2. Analysis of iodine redox-amphoteric conversion. GCD curves of the I_2 electrode at 1 A g^{-1} with varying cutoff voltages in a) $AlCl_3$/EMIMCl and b) in $AlCl_3$/acetamide. c) Raman spectra of $AlCl_3$/EMIMCl before and after 10 GCD cycles at 1 A g^{-1}. d) In situ Raman spectra of the I_2 electrode in $AlCl_3$/acetamide during a charge–discharge cycle. e) I K-edge XANES spectra of the pristine and fully charged I_2 electrode. f) Snapshot from AIMD simulations showing an I^- anion in the $AlCl_3$/acetamide electrolyte. g) Local environment of the I^- anion extracted from the AIMD simulation. Purple sphere: I, blue spheres: Al, green spheres: Cl, red spheres: O, white spheres: H, brown spheres: C, silver spheres: N. h) RDF profile of I–Al pairs extracted from the AIMD simulation.

species with Al–I distance of 4.64 and 4.97 Å (Figure 2h). These findings suggest that I^- is stabilized by forming large ionic clusters with $[AlCl_2{\cdot}(acetamide)_2]^+$ via electrostatic interactions, which are likely immobilized within the porous carbon matrix as the discharged product. The simulations also revealed that ICl molecules can stably exist within the electrolyte environment, and notably, a secondary Cl-containing species such as $[AlCl_3{\cdot}(acetamide)]$ was found to interact with ICl (Figure S10). As ICl is a polar covalent molecule, the iodine atom carries a partial positive charge (δ^+) due to the electronegativity difference between iodine and chlorine. We further calculated the atomic charges of $[AlCl_3{\cdot}(acetamide)]$ by density functional theory (DFT) and found that the chloride atoms carry significant negative charges (Figure S11), enabling them to interact electrostatically with the electrophilic iodine atom from ICl and thereby stabilizing it. This interaction also elongates the I–Cl bond (2.44 Å) compared to free ICl (2.32 Å),[37] leading to the slight red-shift observed in the Raman spectra.

Electrolyte Insights for Iodine Conversion

To elucidate the origin of the differing iodine conversion reversibility across the electrolytes, we evaluated the anodic stability of the four systems using a floating voltage test (Figures S12–15). The stabilized current densities measured at various applied voltages are summarized in Figure 3a. Using 0.01 mA cm^{-2} as the threshold to define electrochemical stability, the ionic liquid electrolytes exhibit limited anodic

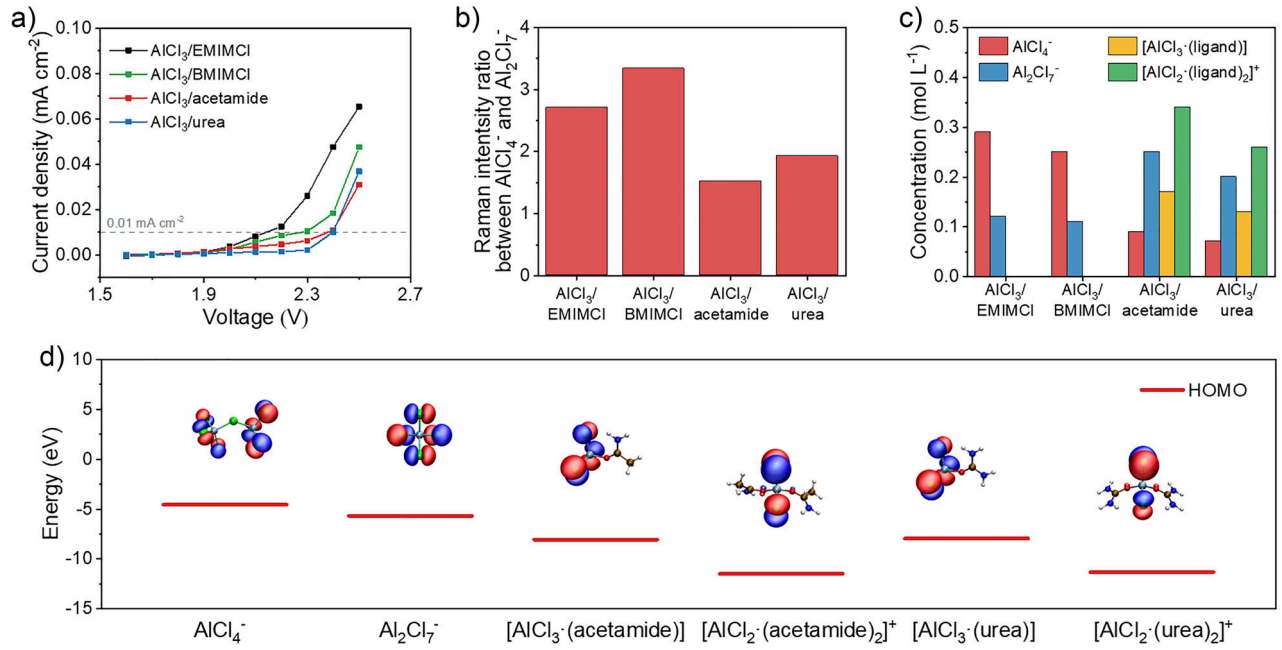

Figure 3. Electrolyte characterizations and simulations. a) Current density as a function of the applied voltage in different electrolytes. b) Raman intensity ratio between $AlCl_4^-$ and $Al_2Cl_7^-$ of different electrolytes. c) Concentration of Cl-contained species in different electrolytes, extracted from AIMD simulations. d) HOMO energy level of different Al–Cl species.

stability, with decomposition initiating below 2.25 V versus Al. In contrast, the eutectic electrolytes exhibit enhanced anodic stability, sustaining voltages up to 2.4 V versus Al. This conclusion was further corroborated by linear sweep voltammetry (LSV) measurements (Figure S16). Notably, Cl_2 generation as a hallmark of oxidative decomposition in ionic liquid electrolytes has previously been identified,[38] aligning with the parasitic reactions observed in Al//I_2 cells employing such electrolytes. Collectively, these findings indicate that the limited reversibility of iodine conversion in ionic liquid systems is primarily attributed to electrolyte decomposition under high-voltage conditions.

We identified the key Al–Cl species in the four electrolytes by ^{27}Al nuclear magnetic resonance (NMR) spectroscopy (Figure S17). As revealed, the two ionic liquid electrolytes exhibit dominant signals corresponding to $AlCl_4^-$ ($\delta = 104.2$ ppm) and $Al_2Cl_7^-$ ($\delta = 98.1$ ppm), consistent with previous reports identifying $AlCl_4^-$ and $Al_2Cl_7^-$ as the dominant Al-species in ionic liquid electrolytes.[39,40] By contrast, the NMR signals of $AlCl_4^-$ and $Al_2Cl_7^-$ are substantially suppressed for the eutectic electrolytes, while additional two strong signals appear at $\delta = 91.1$ ppm and $\delta = 76.0$ ppm, which can be assigned to neutral $[AlCl_3{\cdot}(ligand)]$ species and cationic $[AlCl_2{\cdot}(ligand)_2]^+$ species (ligand = acetamide or urea), respectively.[41] Raman spectra of the four electrolytes reveal that $AlCl_4^-$ species are significantly more abundant in ionic liquid electrolytes than in eutectic electrolytes (Figure S18). This is evidenced by the distinctly higher intensity ratio of the $AlCl_4^-$ to $Al_2Cl_7^-$ Raman peaks in the ionic liquid systems (Figure 3b). In contrast, eutectic electrolytes exhibit a relatively suppressed $AlCl_4^-$ signal, consistent with the reduced concentration of this anion as confirmed by NMR analysis.

Next, AIMD simulations were conducted to provide quantitative insights into the four electrolytes (Figure S19). For ionic liquid electrolytes, the derived RDF profiles around Al atoms reveal the direct Al–Cl coordination (bond length of 2.25 Å) with a coordination number of approximately 4 (Figure S20), aligning with the expected tetrahedral coordination of Al in dominant $AlCl_4^-$ and $Al_2Cl_7^-$ species. By contrast, eutectic electrolytes exhibit a more diverse coordination environment. In addition to the Al–Cl coordination (bond length of 2.25 Å) with an average coordination number of approximately 3.3, a notable Al–O coordination (bond length of 1.85 Å) is observed with an average coordination number of approximately 0.7 (Figures S21–22). This Al–O interaction reflects the presence of $[AlCl_3{\cdot}(ligand)]$ and $[AlCl_2{\cdot}(ligand)_2]^+$ species (where ligand = acetamide or urea). The total coordination number of Al in eutectic electrolytes, combining both Al–Cl and Al–O interactions, remains close to 4, indicating a similarly preferred tetrahedral coordination geometry. Based on the AIMD-derived structures, we further quantified the concentrations of various Al–Cl species (Figure 3c). In line with our Raman spectroscopic analysis, the concentration of $AlCl_4^-$ in eutectic electrolytes is significantly reduced, measured as 0.09 mol L^{-1} for $AlCl_3$/acetamide and 0.07 mol L^{-1} for $AlCl_3$/urea. In contrast, ionic liquid electrolytes show markedly higher $AlCl_4^-$ concentrations, with values of 0.29 mol L^{-1} for $AlCl_3$/EMIMCl and 0.25 mol L^{-1} for $AlCl_3$/BMIMCl.

We further employed DFT calculations to elucidate the decisive species on the oxidative decomposition of the electrolytes, particularly associated with Cl_2 generation in the Al//I_2 cell. Figure 3d displays the energy levels and spatial distribution of the highest occupied molecular orbital

(HOMO) for the primary Al–Cl species. The HOMO distributions (red/blue regions denoting negative/positive phases, respectively) are largely localized around Cl atoms across all Al–Cl species, highlighting their susceptibility to oxidation. This localization implies a strong propensity for electron donation from Cl, potentially leading to Al–Cl bond cleavage and Cl_2 evolution upon oxidation. According to the calculated HOMO energy levels, $AlCl_4^-$ depicts the highest value (−4.55 eV), among all Al–Cl species including $Al_2Cl_7^-$ (−5.67 eV), [$AlCl_3$·(acetamide)] (−8.05 eV), [$AlCl_2$·(acetamide)$_2$]$^+$ (−11.47 eV), [$AlCl_3$·(urea)] (−7.94 eV), and [$AlCl_2$·(urea)$_2$]$^+$ (−11.32 eV). Furthermore, other components present in the electrolytes exhibit HOMO energies well below those of Al–Cl species (Figure S23). This analysis positions the presence of rich $AlCl_4^-$ as the primary reason for electrolyte oxidative decomposition in ionic liquid electrolytes. Meanwhile, due to the deficient presence of $AlCl_4^-$, eutectic electrolytes allow for better anodic stability that is compatible with the I^0/I^+ conversion.

Electrochemical Analysis of the Iodine Electrode

To comprehensively evaluate the electrochemical performance of the I_2 electrode in the optimal $AlCl_3$/acetamide electrolyte, we first collected a series of CV curves at scan rates ranging from 0.1 to 1 mV s^{-1} (Figure 4a). All CV curves present a similar shape with two pairs of redox peaks, corresponding to the I^-/I_2 (O1/R1) and I_2/I^+ (O2/R2) conversion steps. At higher scan rates, the peak current of O2 is not fully captured within the selected potential window due to increased overpotential. Therefore, we initially focused on the peak current densities of the O1/R1 redox pair and plotted log (current density, i) as a function of log (scan rate, v) (Figure 4b). According to Equation 1, the slope of these plots (b-value) serves as an indicator of the underlying electrochemical kinetics.[42–44] Specifically, a b-value of 0.5 signifies a diffusion-controlled process, while a b-value of 1 reveals a surface-controlled capacitive behavior. The extracted b-values of 0.64 (O1) and 0.73 (R1) fall within the intermediate range ($0.5 < b < 1$), suggesting that the redox processes are governed by a mixed mechanism involving both diffusion-controlled and surface-confined charge storage. Electrochemical impedance spectroscopy (EIS) was further measured on the I_2 electrode at various voltages (Figure S24). The derived Ohmic resistance (R_s) and the charge-transfer resistance (R_{ct}) values, obtained by fitting the data to an equivalent circuit model (Figure S25), are summarized in Figure 4c. Notably, R_s remains nearly constant across the tested voltages (around 45 Ω), implying a stable electrode/electrolyte interface. Besides, R_{ct} values stay consistently low under all tested voltages (less than 10 Ω). Compared with the Ketjenblack electrode, which exhibits R_s and R_{ct} of approximately 40 and 5 Ω, respectively (Figure S26), the I_2 electrode exhibits comparable R_s and R_{ct} values, indicating fast charge-transfer kinetics and excellent interfacial electrochemical reversibility of the iodine redox–amphoteric conversion.

$$i = av^b \quad (0.5 \leq b \leq 1) \tag{1}$$

GCD curves at various current densities were further collected to evaluate the rate capability of the I_2 electrode (Figure 4d). At 0.5 mA g^{-1}, the I_2 electrode reaches a specific capacity of 389 mAh g^{-1}, referring to a 92% utilization efficiency of active I_2 (theoretically 422 mAh g^{-1}). Together with an average discharge voltage of 1.37 V, the I_2 electrode delivers a high energy density of 533 Wh kg^{-1} (based on the I_2 mass), substantially outperforming most reported cathode materials (Figure 4e & Table S1), such as graphite foam (147 Wh kg^{-1}),[8] natural graphite (220 Wh kg^{-1}),[45] graphene (190 Wh kg^{-1}),[11] V_2CT_x (154 Wh kg^{-1}),[46] MOF (177 Wh kg^{-1}),[47] Co_9S_8 (268 Wh kg^{-1}),[18] VO_2 (46 Wh kg^{-1}),[48] P-V_2O_5 (466 Wh kg^{-1}),[49] $MoSe_2$ (55 Wh kg^{-1}),[50] $FeWO_4$ (256 Wh kg^{-1}),[51] PQ-triangle (252 Wh kg^{-1}),[20] amine (138 Wh kg^{-1}),[52] polypyrene (170 Wh kg^{-1}),[53] NT-COF (172 Wh kg^{-1}),[40] and iodine (I^-/I^0) (158 Wh kg^{-1}).[28] Even at a high current density of 2 A g^{-1}, the I_2 electrode still maintains a considerable specific capacity of 264 mAh g^{-1}, indicating a high I_2 utilization efficiency of 63%. In addition, we evaluated the symmetric Al//Al cells under these equivalent areal current densities. As shown in Figure S27, the average voltage polarization is only 140 mV at a small current density of 1 mA cm−2. At a high current density of 4 mA cm−2, the average voltage polarization reaches 350 mV. This result reflects that the observed voltage polarization in the Al//I_2 cell mainly comes from the Al anode reaction.

The long-term cycling stability of the I_2 electrode was further evaluated through the GCD measurement at 1 A g^{-1}. As shown in Figure 4f, the electrode retains 83.8% of its initial capacity after 1000 cycles, corresponding to a low decay rate of 0.016% per cycle. The observed fluctuation is likely due to variations in ambient temperature. This cycling stability clearly surpasses that of other reported conversion-type cathodes for Al batteries, such as S (28.1% retention after 200 cycles, decay rate of 0.359% per cycle),[54] Se (26% retention after 200 cycles, decay rate of 0.370% per cycle),[55] and Te (61% retention after 20 cycles, decay rate of 1.950% per cycle).[56] The excellent cycling stability is primarily ascribed to the suppression of iodine species shuttling by the $AlCl_3$/acetamide electrolyte. As shown in Figure S28, separators from cycled Al//I_2 cells using $AlCl_3$/EMIMCl in this electrolyte exhibited no visible color change, confirming the effective inhibition of polyiodide shuttling, whereas pronounced reddish discoloration was observed for separators collected in $AlCl_3$/EMIMCl. Moreover, scanning electron microscope (SEM) and corresponding energy-dispersive X-ray (EDX) analysis of the Al anode cycled in $AlCl_3$/acetamide revealed only Al signals without detectable iodine (Figure S29), further corroborating the suppression of the shuttle effect in the $AlCl_4^-$-deficient eutectic electrolytes.

High-Loading Iodine Electrodes and Device Demonstration

The promising performance of iodine conversion further motivated us to fabricate high-loading I_2 electrodes aimed at enhancing areal capacity toward practical applications. A series of electrodes with varying I_2 loading masses

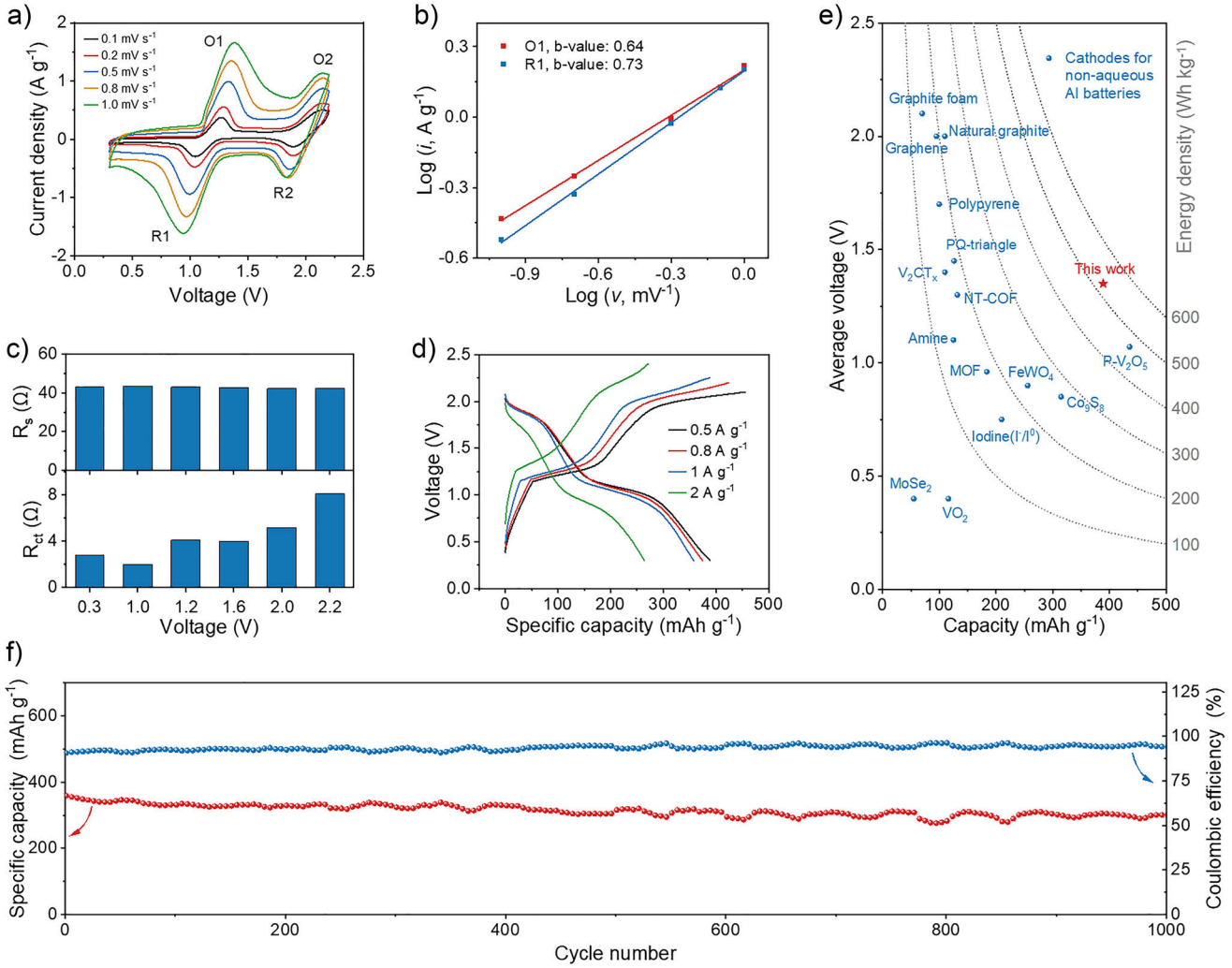

Figure 4. Electrochemical analysis of the I_2 electrode. a) CV curves of the I_2 electrode at various scan rates. b) Log(i) as a function of log(v) for the O1/R1 peaks of the I_2 electrode. c) R_s and R_{ct} of the I_2 electrode derived from the EIS analysis of the I_2 electrode at different voltages. d) GCD profiles of the I_2 electrode at different current densities. e) The average discharge voltage and specific capacity of the I_2 electrode in comparison with reported cathode materials for non-aqueous Al batteries. f) Cycling performance of the I_2 electrode at 1 A g^{-1}.

were prepared and evaluated with the GCD measurement at 2 mA cm^{-2}. Benefiting from the fast kinetics of the iodine redox-amphoteric conversion, the I_2 cathodes exhibited two distinct voltage plateaus and delivered high capacities across a wide range of mass loadings from 2.25 to 8.52 mAh cm^{-2} (Figure S30). Figure 5a plots the calculated gravimetric capacity and areal capacity as a function of the loading mass. Along the loading mass increased from 2.26 to 4.43 mg cm^{-2}, the gravimetric capacity slightly decreased from 357 to 331 mAh g^{-1}, while the areal capacity correspondingly increased from 0.81 to 1.47 mAh cm^{-2}. At a high loading of 8.52 mg cm^{-2}, the gravimetric capacity declined further to 265 mAh g^{-1}, yet the areal capacity reached up to 2.25 mAh cm^{-2}. This areal capacity ranks among the highest reported for Al battery cathodes (Figure 5b), surpassing benchmark materials such as graphite (0.38 mAh cm^{-2}),[45] graphene (1.24 mAh cm^{-2}),[11] 2D Cu-based MOF (0.18 mAh cm^{-2}),[47] 4,4′,4″-tris(diphenylamino)triphenylamine (1.61 mAh cm^{-2}),[52] Te (0.91 mAh cm^{-2}),[56] S (1.60 mAh cm^{-2}),[19] V_2CT_x (0.51 mAh cm^{-2}),[46] and Co_9S_8 (0.47 mAh cm^{-2}).[18] Notably, the high-loading I_2 electrode (8.52 mg cm^{-2}) also demonstrated excellent cycling stability, retaining 80.4% of its initial capacity after 600 cycles (Figure S31).

To demonstrate the practicability of the high-loading I_2 electrode (~ 8 mg cm^{-2}), we further assembled a single-layer pouch cell (4 × 5 cm^2) by coupling with a piece of Al foil anode (25 μm in thickness). As shown in Figure 5c, the assembled device was able to achieve a capacity of 35 mAh at a current density of 2 mA cm^{-2}. Additionally, the pouch cell exhibited good rechargeability over 100 cycles (Figure 5d) and was capable of powering a digital timer requiring 1.5 V (Figure 5e). All these results underscore the potential of the Al–I_2 cell as a promising energy storage device suited for future large-scale energy storage applications.

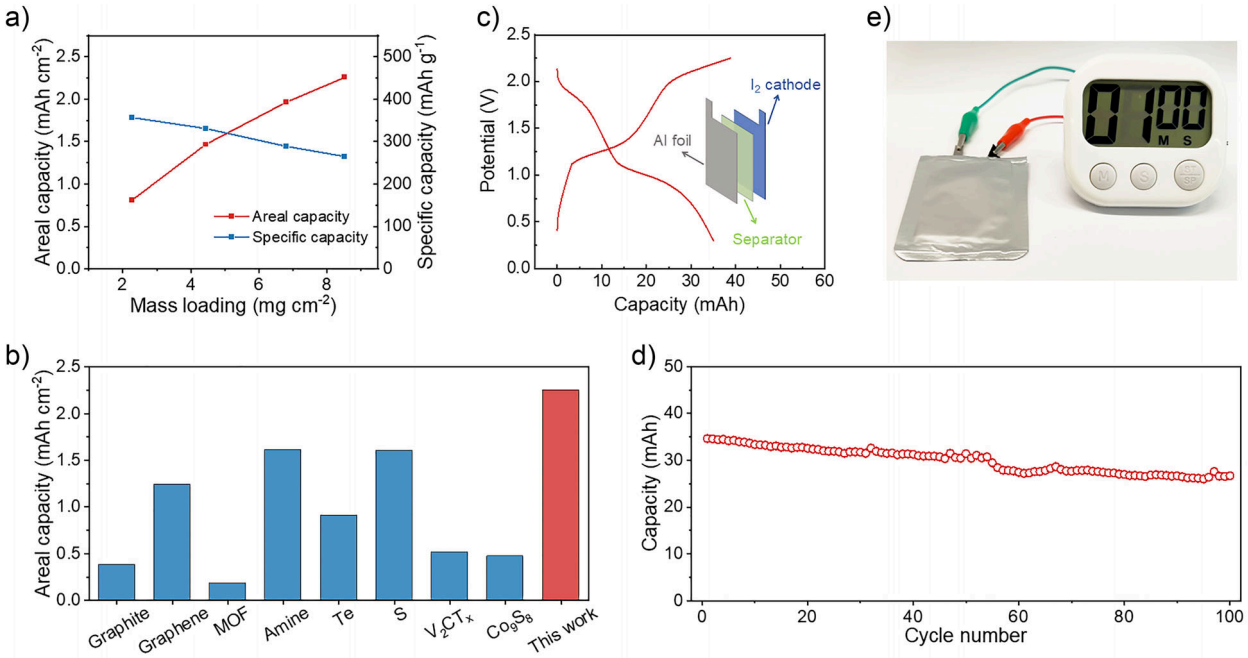

Figure 5. Electrochemical performance of high-loading I_2 electrodes and pouch-cell device. a) Areal and specific capacities of the I_2 electrodes with different loading masses. b) Areal capacity of the high-loading I_2 electrode (8.52 mg cm^{-2}) in comparison with recently reported cathodes for non-aqueous Al batteries. c) GCD curves of the single-layer Al–I_2 pouch cell at 2 mA cm^{-2}. The inset illustrates the device configuration. d) Cycling performance of the single-layer Al–I_2 pouch cell at 2 mA cm^{-2}. e) Digital photo of a timer powered by an Al–I_2 pouch cell.

Conclusion

In summary, we have unlocked the reversible iodine redox-amphoteric conversion ($I^-/I^0/I^+$) in Al batteries and disclosed the critical role of $AlCl_4^-$-deficient eutectic electrolytes. Unlike ionic liquid systems, which suffered from parasitic Cl_2 evolution and low Coulombic efficiency, eutectic electrolytes offered a wider anodic stability window and enabled the I_2 electrode to achieve $I^-/I^0/I^+$ conversion, delivering a high specific capacity of 358 mAh g^{-1} at 1 A g^{-1}. This favorable electrochemical behavior was attributed to the suppressed concentration of $AlCl_4^-$, identified as the dominant species governing the oxidative stability of the electrolyte. The efficient and desirable $I^-/I^0/I^+$ conversion chemistry further allowed the construction of high-loading I_2 electrodes, which delivered an unprecedented areal capacity of 2.25 mAh cm^{-2}, surpassing all previously reported cathodes for non-aqueous Al batteries. The proposed amphoteric iodine redox mechanism introduces a new design strategy for developing energy-dense aluminum battery systems. Meanwhile, we acknowledged the remaining challenges in the constructed Al//I_2 cell, particularly the need for improvement in its Coulombic efficiency. Addressing this limitation will require substantial future efforts focused on system-level optimization, including the rational design of host materials and further advancement in electrolyte engineering.

Acknowledgements

This work was financially supported by European Union's Horizon Europe research and innovation programme (LEAF 101186701), German Research Foundation (DFG) within the Cluster of Excellence, and CRC 1415 (Grant No. 417590517). X.C. was supported by a grant from the China Scholarship Council (File No. 202108060037). The authors acknowledge the use of the facilities in the Dresden Center for Nanoanalysis (DCN) at the Technische Universität Dresden, the GWK support for providing computing time through the Center for Information Services and High-Performance Computing (ZIH) at TU Dresden, beam time allocation at beamline P65 at the PETRA III synchrotron (DESY, Hamburg, Germany) and beamline BL22 at ALBA Synchrotron, Barcelona, Spain.

Open access funding enabled and organized by Projekt DEAL.

Conflict of Interests

The authors declare no conflict of interest.

Data Availability Statement

The data that support the findings of this study are available from the corresponding author upon reasonable request.

Keywords: Aluminum batteries · Eutectic electrolytes · Iodine cathodes · Iodine conversion · Redox amphoteric

[1] H. Yang, H. Li, J. Li, Z. Sun, K. He, H.-M. Cheng, F. Li, *Angew. Chem. Int. Ed.* **2019**, *58*, 11978–11996.
[2] J. Tu, W.-L. Song, H. Lei, Z. Yu, L.-L. Chen, M. Wang, S. Jiao, *Chem. Rev.* **2021**, *121*, 4903–4961.

[3] G. A. Elia, K. Marquardt, K. Hoeppner, S. Fantini, R. Lin, E. Knipping, W. Peters, J.-F. Drillet, S. Passerini, R. Hahn, *Adv. Mater.* **2016**, *28*, 7564–7579.
[4] Y. Zhang, S. Liu, Y. Ji, J. Ma, H. Yu, *Adv. Mater.* **2018**, *30*, 1706310.
[5] Q. Pang, J. Meng, S. Gupta, X. Hong, C. Y. Kwok, J. Zhao, Y. Jin, L. Xu, O. Karahan, Z. Wang, S. Toll, L. Mai, L. F. Nazar, M. Balasubramanian, B. Narayanan, D. R. Sadoway, *Nature* **2022**, *608*, 704–711.
[6] Q. Guo, H. Xu, X. Chu, X. Huang, M. Yu, X. Feng, *Chem. Soc. Rev.* **2025**, *54*, 4035–4086.
[7] M. Angell, C.-J. Pan, Y. Rong, C. Yuan, M.-C. Lin, B.-J. Hwang, H. Dai, *Proc. Natl. Acad. Sci. U.S.A.* **2017**, *114*, 834–839.
[8] M.-C. Lin, M. Gong, B. Lu, Y. Wu, D.-Y. Wang, M. Guan, M. Angell, C. Chen, J. Yang, B.-J. Hwang, H. Dai, *Nature* **2015**, *520*, 324–328.
[9] M. Jiang, C. Fu, P. Meng, J. Ren, J. Wang, J. Bu, A. Dong, J. Zhang, W. Xiao, B. Sun, *Adv. Mater.* **2022**, *34*, 2102026.
[10] E. Fuentes-Mendoza, M. Talari, E. Zemlyanushin, R. Cordoba, N. Sabi, S. Dsoke, *ChemElectroChem* **2025**, *12*, e202400705.
[11] H. Chen, H. Xu, S. Wang, T. Huang, J. Xi, S. Cai, F. Guo, Z. Xu, W. Gao, C. Gao, *Sci. Adv.* **2017**, *3*, eaao7233.
[12] X. Chu, J. Du, J. Zhang, X. Li, X. Liu, Y. Wang, J. Hunger, A. Morag, J. Liu, Q. Guo, D. Li, Y. Han, M. Bonn, X. Feng, M. Yu, *Nat. Commun.* **2025**, *16*, 6329.
[13] B.-E. Jia, A. Q. Thang, C. Yan, C. Liu, C. Lv, Q. Zhu, J. Xu, J. Chen, H. Pan, Q. Yan, *Small* **2022**, *18*, 2107773.
[14] H. Xu, H. Chen, H. Lai, Z. Li, X. Dong, S. Cai, X. Chu, C. Gao, *J. Energy Chem.* **2020**, *45*, 40–44.
[15] K. L. Ng, B. Amrithraj, G. Azimi, *Joule* **2022**, *6*, 134–170.
[16] Z. Zhu, T. Jiang, M. Ali, Y. Meng, Y. Jin, Y. Cui, W. Chen, *Chem. Rev.* **2022**, *122*, 16610–16751.
[17] E. Faegh, B. Ng, D. Hayman, W. E. Mustain, *Nat. Energy* **2021**, *6*, 21–29.
[18] Y. Hu, D. Ye, B. Luo, H. Hu, X. Zhu, S. Wang, L. Li, S. Peng, L. Wang, *Adv. Mater.* **2018**, *30*, 1703824.
[19] T. Gao, X. Li, X. Wang, J. Hu, F. Han, X. Fan, L. Suo, A. J. Pearse, S. B. Lee, G. W. Rubloff, K. J. Gaskell, M. Noked, C. Wang, *Angew. Chem. Int. Ed.* **2016**, *55*, 9898–9901.
[20] D. J. Kim, D.-J. Yoo, M. T. Otley, A. Prokofjevs, C. Pezzato, M. Owczarek, S. J. Lee, J. W. Choi, J. F. Stoddart, *Nat. Energy* **2019**, *4*, 51–59.
[21] F. Ambroz, T. J. Macdonald, T. Nann, *Adv. Energy Mater.* **2017**, *7*, 1602093.
[22] K. Du, Y. Liu, Y. Zhao, H. Li, H. Liu, C. Sun, M. Han, T. Ma, Y. Hu, *Adv. Mater.* **2024**, *36*, 2404172.
[23] X. Li, Y. Shen, X. Wang, S. Ni, L. Yue, S. A. Khan, J. Zhao, J. Xu, *Energy Storage Mater.* **2024**, *71*, 103660.
[24] Z. Cheng, H. Pan, F. Li, C. Duan, H. Liu, H. Zhong, C. Sheng, G. Hou, P. He, H. Zhou, *Nat. Commun.* **2022**, *13*, 125.
[25] F. Wang, Z. Liu, C. Yang, H. Zhong, G. Nam, P. Zhang, R. Dong, Y. Wu, J. Cho, J. Zhang, X. Feng, *Adv. Mater.* **2020**, *32*, 1905361.
[26] S. Zhao, B. Zhang, L. Li, P. Zhang, G. Li, Z. Zhu, Y. Choi, L. Dong, M. Luo, S. Guo, *J. Am. Chem. Soc.* **2025**, *147*, 669–677.
[27] J. Hao, L. Yuan, Y. Zhu, X. Bai, C. Ye, Y. Jiao, S.-Z. Qiao, *Angew. Chem. Int. Ed.* **2023**, *62*, e202310284.
[28] H. Tian, S. Zhang, Z. Meng, W. He, W.-Q. Han, *ACS Energy Lett.* **2017**, *2*, 1170–1176.
[29] Y. Zou, T. Liu, Q. Du, Y. Li, H. Yi, X. Zhou, Z. Li, L. Gao, L. Zhang, X. Liang, *Nat. Commun.* **2021**, *12*, 170.
[30] R. L. Aggarwal, L. W. Farrar, S. Di Cecca, T. H. Jeys, *AIP Adv.* **2016**, *6*, 025310.
[31] V. A. Elterman, P. Y. Shevelin, L. A. Yolshina, E. G. Vovkotrub, A. V. Borozdin, *J. Mol. Liq.* **2020**, *320*, 114482.
[32] S. Zhang, X. Tan, Z. Meng, H. Tian, F. Xu, W.-Q. Han, *J. Mater. Chem. A* **2018**, *6*, 9984–9996.
[33] P. Klaeboe, *J. Am. Chem. Soc.* **1967**, *89*, 3667–3676.
[34] X. Li, Y. Wang, Z. Chen, P. Li, G. Liang, Z. Huang, Q. Yang, A. Chen, H. Cui, B. Dong, H. He, C. Zhi, *Angew. Chem. Int. Ed.* **2022**, *61*, e202113576.
[35] J. G. Parsons, M. V. Aldrich, J. L. Gardea-Torresdey, *Appl. Spectrosc. Rev.* **2002**, *37*, 187–222.
[36] S. Kodama, Y. Takahashi, K. Okumura, T. Uruga, *Sci. Total Environ.* **2006**, *363*, 275–284.
[37] A. Kalemos, R. Prosmiti, *J. Chem. Phys.* **2014**, *141*, 104312.
[38] H. Xu, T. Bai, H. Chen, F. Guo, J. Xi, T. Huang, S. Cai, X. Chu, J. Ling, W. Gao, Z. Xu, C. Gao, *Energy Storage Mater.* **2019**, *17*, 38–45.
[39] C. Ferrara, V. Dall'Asta, V. Berbenni, E. Quartarone, P. Mustarelli, *J. Phys. Chem. C* **2017**, *121*, 26607–26614.
[40] Y. Liu, Y. Lu, A. Hossain Khan, G. Wang, Y. Wang, A. Morag, Z. Wang, G. Chen, S. Huang, N. Chandrasekhar, D. Sabaghi, D. Li, P. Zhang, D. Ma, E. Brunner, M. Yu, X. Feng, *Angew. Chem.Int. Ed.* **2023**, *62*, e202306091.
[41] P. Hu, R. Zhang, X. Meng, H. Liu, C. Xu, Z. Liu, *Inorg. Chem.* **2016**, *55*, 2374–2380.
[42] B. Sun, Q. Lu, K. Chen, W. Zheng, Z. Liao, N. Lopatik, D. Li, M. Hantusch, S. Zhou, H. I. Wang, Z. Sofer, E. Brunner, E. Zschech, M. Bonn, R. Dronskowski, D. Mikhailova, Q. Liu, D. Zhang, M. Yu, X. Feng, *Adv. Mater.* **2022**, *34*, 2108682.
[43] A. Morag, X. Chu, C. Neumann, D. Pohl, M. Borrelli, D. Sabaghi, M. Löffler, Z. Sofer, A. Turchanin, M. Yu, X. Feng, *Energy Storage Mater.* **2022**, *53*, 435–443.
[44] K. Du, Y. Liu, Y. Yang, F. Cui, J. Wang, M. Han, J. Su, J. Wang, X. Han, Y. Hu, *Adv. Mater.* **2023**, *35*, 2301538.
[45] G. A. Elia, N. A. Kyeremateng, K. Marquardt, R. Hahn, *Batter. Supercaps* **2019**, *2*, 83–90.
[46] A. VahidMohammadi, A. Hadjikhani, S. Shahbazmohamadi, M. Beidaghi, *ACS Nano* **2017**, *11*, 11135–11144.
[47] Y. Guo, W. Wang, H. Lei, M. Wang, S. Jiao, *Adv. Mater.* **2022**, *34*, 2110109.
[48] W. Wang, B. Jiang, W. Xiong, H. Sun, Z. Lin, L. Hu, J. Tu, J. Hou, H. Zhu, S. Jiao, *Sci. Rep.* **2013**, *3*, 3383.
[49] F. Cui, J. Li, C. Lai, C. Li, C. Sun, K. Du, J. Wang, H. Li, A. Huang, S. Peng, Y. Hu, *Nat. Commun.* **2024**, *15*, 8108.
[50] J. Guo, S. Gu, W. Nie, B. Long, S. Ryazantsev, S. Malyshev, J. Li, S. Guo, C. Wu, *Adv. Mater.* **2025**, *37*, 2419865.
[51] H. Wang, Y. Li, B. Long, S. Li, X. Lu, S. Zhou, F. Wu, Y. Bai, C. Wu, *Angew. Chem. Int. Ed.* **2025**, *64*, e202510773.
[52] G. Wang, E. Dmitrieva, B. Kohn, U. Scheler, Y. Liu, V. Tkachova, L. Yang, Y. Fu, J. Ma, P. Zhang, F. Wang, J. Ge, X. Feng, *Angew. Chem. Int. Ed.* **2022**, *61*, e202116194.
[53] M. Walter, K. V. Kravchyk, C. Böfer, R. Widmer, M. V. Kovalenko, *Adv. Mater.* **2018**, *30*, 1705644.
[54] Y. Guo, Z. Hu, J. Wang, Z. Peng, J. Zhu, H. Ji, L.-J. Wan, *Angew. Chem.Int. Ed.* **2020**, *59*, 22963–22967.
[55] T. Zhang, T. Cai, W. Xing, T. Li, B. Liang, H. Hu, L. Zhao, X. Li, Z. Yan, *Energy Storage Mater.* **2021**, *41*, 667–676.
[56] H. Jiao, D. Tian, S. Li, C. Fu, S. Jiao, *ACS Appl. Energy Mater.* **2018**, *1*, 4924–4930.

Manuscript received: July 22, 2025
Revised manuscript received: September 02, 2025
Manuscript accepted: September 18, 2025
Version of record online: October 05, 2025